ELSEVIER

Contents lists available at ScienceDirect

Earth and Planetary Science Letters

journal homepage: www.elsevier.com/locate/epsl



A shallow slow slip event in 2018 in the Semidi segment of the Alaska subduction zone detected by machine learning



Bing He^{a,*}, XiaoZhuo Wei^a, Meng (Matt) Wei^{a,*}, Yang Shen^a, Marco Alvarez^b, Susan Y. Schwartz^c

- ^a Graduate School of Oceanography, University of Rhode Island, United States of America
- ^b Department of Computer Science and Statistics, University of Rhode Island, United States of America
- ^c Earth and Planetary Sciences Department, University of California, Santa Cruz, United States of America

ARTICLE INFO

Article history:

Received 27 October 2022

Received in revised form 26 March 2023

Accepted 1 April 2023 Available online xxxx Editor: J.P. Avouac

Dataset link: https://www.hycom.org/dataserver/gofs-3pt1/reanalysis

Dataset link: https://

podaac.jpl.nasa.gov/ECCO?tab=mission-objectives§ions=about%2Bdata

Dataset link: https://

www.gmrt.org/GMRTMapTool/

Dataset link: https://keras.io/

Dataset link: https://sci-kit-learn.org/stable/
Dataset link: https://github.com/bing-he/
SSE_detection_using_machine_learning

Keywords: slow slip events machine learning seafloor pressure data Alaska

great earthquakes and tsunamis

ABSTRACT

Slow slip events (SSEs) have been discovered at shallow depth near the trench in some subduction zones and have been linked to the triggering of large earthquakes and the absence of tsunami. These shallow SSEs are invariably submarine, making it difficult to observe their temporal and spatial extent. Here, we report a shallow SSE in late 2018 near the west Semidi segment of the Alaska subduction zone, up-dip of and preceding the Mw 8.2 Chignik earthquake on July 29th, 2021. The SSE was detected in data from an offshore array of seafloor pressure gauges by a machine learning method. This detection is supported by the spatial pattern of simulated SSE deformation, the increased seismicity after the SSE in the positive Coulomb stress change area, the lack of shallow slip in Chignik earthquake, and the absence of a sizable tsunami following the Chignik earthquake. Our method has the potential to transform the way offshore SSEs are detected and to improve tsunami hazard assessment in subduction zones.

© 2023 Elsevier B.V. All rights reserved.

1. Introduction

1.1. Shallow slow slip events

Slow slip events (SSEs) have recently been discovered at shallow depth on the plate interface in some subduction zones, including Costa Rica and New Zealand (Araki et al., 2017; Davis et al., 2015, p. 2; Dixon et al., 2014; Saffer and Wallace, 2015; Wallace et al., 2016). These shallow SSEs may be linked to tsunamigenic

earthquakes and the triggering of large interplate earthquakes (Hino et al., 2014; Ito et al., 2013; Saffer and Wallace, 2015). SSEs likely play an important but as yet unresolved role in the accommodation of plate motion near the trench at many subduction zones. Detailed observations of slip during SSEs are critical to understand the distribution of locking on subduction faults offshore, which determines the potential seismic and tsunami hazard posed by subduction zones (Lindsey et al., 2021). However, it is challenging to detect and measure shallow SSEs because the standard GNSS systems for measuring land displacement do not operate under water. Seafloor pressure gauges, which detect SSEs by observing pressure changes due to vertical displacement of the seafloor, currently provide the only viable way to continuously observe and

^{*} Corresponding authors.

E-mail addresses: bing-he@uri.edu (B. He), matt-wei@uri.edu (M. Wei).

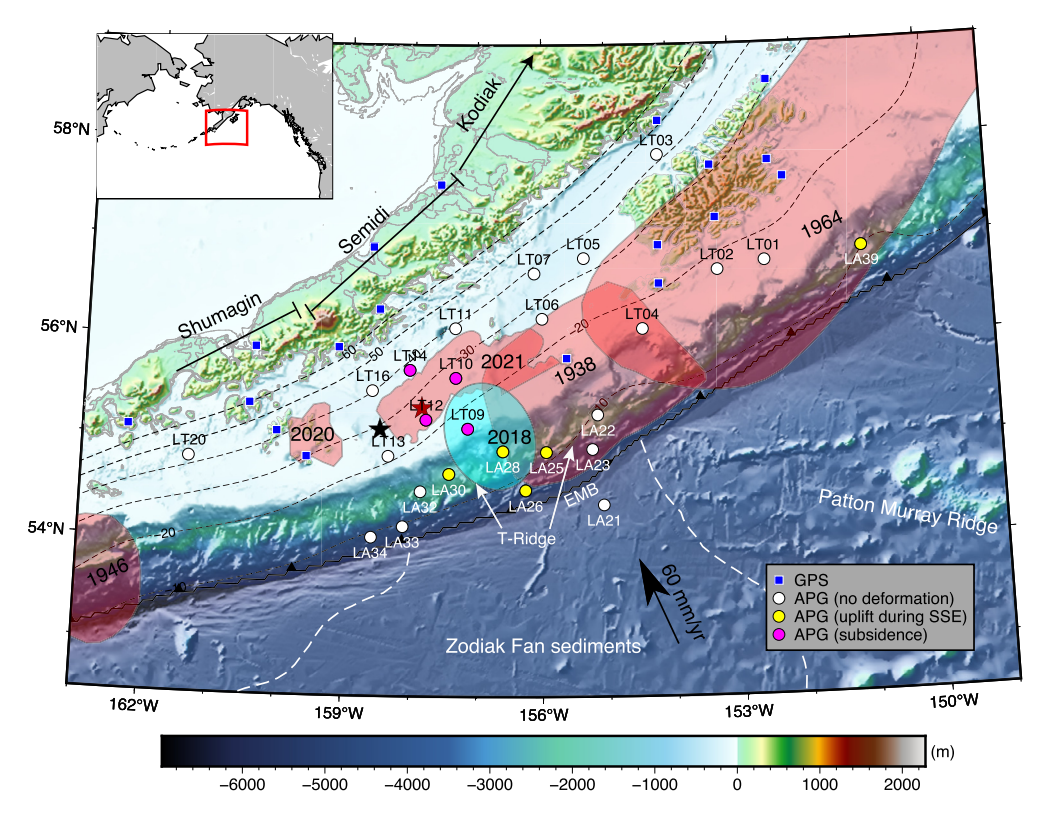


Fig. 1. Map of the study area along the Alaska-Aleutian megathrust (the red box in the small inset on the top left). White, magenta, and yellow circles represent absolute pressure gauges (APGs) in AACSE. The dashed black lines indicate the slab depth contours with a 10 km interval from Slab2 (Hayes et al., 2018). The red shaded areas are the historical earthquake distributions. Slip of 1 m is outlined from the best fitting models of Freymueller et al. (2021) for the 1938 Mw 8.3 Semidi earthquake, Crowell and Melgar (2020) for the July 22, 2020 Mw 7.8 Simeonof earthquake and Ye et al. (2022) for the July 29, 2021 Mw 8.2 Chignik earthquake. The black and red stars label the epicenters of the 2020 Simeonof earthquake and 2021 Chignik earthquake, respectively. The cyan shaded area is our preferred 2018 SSE area. The white dashed lines show the area covered by Zodiak Fan sediments. T-ridge represents the transitional ridge or escapement terminating the transitional zone. EMB means the embayment into the Semidi deformation front (von Huene et al., 2016).

spatially map out displacements during a near-trench SSE (Ito et al., 2013; Ruiz et al., 2014; Wallace et al., 2016). The challenge is that oceanic noise is comparable to the tectonic signal in seafloor pressure data and only very large SSEs with several centimeters of seafloor displacement can be observed (Fredrickson et al., 2019; Wallace et al., 2016).

Recently, we developed a machine learning method to detect small and shallow SSEs in seafloor pressure data (He et al., 2020). We have applied this method to data in New Zealand between 2014 and 2015 and detected five events, two of which are confirmed by the onshore GNSS records. We also have shown that our method performs better than the traditional matched filter method (He et al., 2020). Here, we improved the method by adding the capability of detecting not only seafloor uplift but also subsidence. We applied this improved method to the seafloor pressure data collected in the Alaska Amphibious Community Seismic Experiment (AACSE) (Fig. 1). The spatial pattern of the vertical deformation in late October 2018 is consistent with an SSE. The occurrence of an SSE is also supported by seismicity patterns around the event and the lack of shallow slip and tsunami in the 2021 Mw 8.2 Chignik earthquake. The unique geological structure of the seafloor in this area may create favorable conditions for SSEs.

1.2. Earthquakes and SSEs in Alaska

The Alaska subduction zone in the study region shows diverse slip behaviors, incoming plate structures, and hydration levels (S. Li and Freymueller, 2018; S. S. Wei et al., 2021). In the west, the Shumagin segment shows a low degree of seismic locking, called the Shumagin gap (Davies et al., 1981), which has abundant seismicity but lacks large earthquakes. The 2020 Mw 7.8 earthquake was the

largest event in the eastern Shumagin gap since 1917 (Crowell and Melgar, 2020). No shallow slip was released by this earthquake and its aftershocks, and most slip was at depths between 20 and 45 km (Liu et al., 2020; Xiao et al., 2021; Ye et al., 2021). The Semidi segment is in the middle of the Shumagin and Kodiak segments and can host large earthquakes with a magnitude over 8 every 50 to 75 years (Davies et al., 1981). The last two events were the 1938 M 8.3 earthquake and the 2021 Mw 8.2 Chignik earthquake. There is no seismic slip model for the 1938 earthquake, but the aftershock zone extended ~270-300 km along strike and a tsunami model showed large slip concentrated at shallow depth (< 20 km) (Davies et al., 1981; Freymueller et al., 2021). The 2021 earthquake had about half of its slip overlapping with the 1938 earthquake rupture with most slip occurring deeper than 20 km (Liu et al., 2022; Ye et al., 2022). The Semidi segment is characterized as having intermediate locking, with more sediments subducted, resulting in smoother seafloor than the Shumagin segment (J. Li et al., 2015; S. Li and Freymueller, 2018; Shillington et al., 2015). The Kodiak segment shows high locking and has the most active seismicity at all depths (S. Li and Freymueller, 2018; S.S. Wei et al., 2021). The Kodiak segment and eastward hosted the great 1964 M 9.2 earthquake. The systematic along-strike variations provide an excellent opportunity to explore the relationship between earthquake behavior and geological/geophysical setting.

In both Upper and Lower Cook Inlet, in south-central Alaska, long-term SSEs with durations of a couple of years and intervals of several years have been observed for the last 25 years. The duration, interval, and magnitude of these SSEs vary from event to event, but these SSEs occur at a depth of around 40 km to 60 km, which coincides with the down-dip limit of megathrust earth-

quakes (S. Li et al., 2016; M. Wei et al., 2012). So far, no SSE has been reported in the Kodiak to Shumagin segments.

2. Materials and methods

2.1. AACSE pressure data preprocessing

Between May 2018 and August 2019, AACSE deployed 75 broad-band ocean-bottom seismometers (OBSs) and 30 broad-band land seismometers on the southern Alaskan subduction margin, aiming to study tectonics, structure, and seismicity (Barcheck et al., 2020) (Fig. S1). 34 of the OBSs were equipped with absolute pressure gauges (APGs). Among the 34 APGs, we used data from 15 shallow-water (depth < 300 m) and 11 deep-water stations (depth > 1500 m) that had data archived at IRIS (Fig. 1). The APGs at stations LA26, LT02, and LT09 stopped recording midway through the deployment and therefore have much less data than the other stations. The sampling rate of the raw data is 120 Hz. We down-sampled to one sample per 30 minutes since the high-frequency content is not relevant to our study.

We processed the seafloor pressure data in three steps: detiding, de-drifting, and removing oceanographic signals. First, we removed tides using tidal response analysis (Munk et al., 1966) (Fig. S2a). Second, we used an improved method to remove the sensor drift. Pressure sensor drift is a gradual sensor degradation, which is traditionally estimated using an exponential plus linear curve (Watts and Kontoyiannis, 1990). However, we found that the conventional method over-estimated the drift by including long-period (30~200 days) ocean signals. Therefore, we modified the conventional method with the help of the ocean circulation model, HYCOM, which can reasonably predict the long-period ocean waves. We first subtracted the low pass filtered (fourthorder Butterworth filter with 20 days) HYCOM data from the detided pressure data, and then we used the conventional method to remove the drift. Then, we added the HYCOM data back to the dedrifted pressure data (Fig. S2b). Even though the new de-drifted method has a slightly higher RMS (root mean square), it shows a higher correlation coefficient with HYCOM data than the conventional method (Fig. S2cd and S3) because the new de-drifting approach can remove the drift without affecting the long-period ocean waves.

Third, because of the large difference in their ocean circulation patterns, we removed oceanographic noise separately from the shallow and deep water stations. The deep ocean system is relatively quiet and less affected by wind stress than the shallow ocean system. The eddies in the deep ocean can reach lateral scales of several hundreds of kilometers and larger. We thus assumed most deep-water stations are affected by identical deep eddy flows. Following the reference station method (Wallace et al., 2016), we subtracted station LA21 located on the other side of the trench from all deep-water stations. The shallow ocean system is primarily affected by wind forcing and atmospheric pressure loading. By comparing the shallow water pressures, we found that although the shallow water stations record the same period of ocean waves, they have various amplitudes. If we choose one-referencestation subtraction method, some oceanographic signals would be left or over-subtracted by the reference station. Therefore, instead of using the reference method, we subtract the HYCOM ocean circulation model for the shallow water stations. We tested both the HYCOM and ECCO4 ocean circulation models. The spatial resolution of HYCOM (1/12 degrees) is finer than ECCO4 (0.5 degrees) resulting in correlation coefficients between HYCOM and real pressure data significantly higher than ECCO4. There are other ways to remove oceanographic noise in seafloor pressure data including global mean, isobath average, temperature and pressure correlation (Fredrickson et al., 2019; Gomberg et al., 2019; Hino et al., 2014; Inazu et al., 2012). In this study, we also found that the global mean method was unsuitable for an area as large as this study. The average isobath removal method is difficult to implement, and it may result in removing some of the geodetic signal. In addition, the temperature and pressure correlation method did not improve the variance reduction for this study.

Fig. S4A shows the shallow-water comparison between the real seafloor pressure data and HYCOM. Fig. S4B shows the deep-water residual comparison. HYCOM performs better on the continental shelf than on the steep continental slope because of the rapid water movements on the slope. Here we filtered the real pressure and HYCOM data using a 1-day low pass filter, removing the high frequency signals to improve data comparison.

We calculated the variance reduction (VR) to describe how much oceanographic signals can be removed in seafloor pressure data (Fig. S5). $VR = \frac{1-(Variance(Real-HYCOM))}{Variance(Real)}$. For shallow-water stations, with the exception of the very noisy station LT05, the average correlation coefficient (CC) between the real seafloor pressure and HYCOM output is 0.80. The average VR is 0.64. For deep-water stations, the average CC is 0.82, and the average VR is 0.70. We also tried different low pass filters from one to ten days in HYCOM pressure data and the result did not improve. The variance reductions in this study are comparable to results obtained in New Zealand (Muramoto et al., 2019), even though the station spacing in Alaska is greater. The variance of the pressure data was reduced to a few centimeters equivalent from tens of centimeters. This pressure difference is the data we put into the machine learning detector.

2.2. SSE detection with machine learning

We built a deep learning model to detect the approximate time of SSEs in the pressure records. The basic procedure is the same as in our previous study (He et al., 2020). Here we added the capability of detecting subsidence as well as uplift. Because real seafloor pressure data are limited and insufficient, we used synthetic data to train the machine learning model (detector). The synthetic data have a spectrum similar to the real data and contain the expected SSE signals with random duration, amplitude, and timing. We evaluated the model performance and applied the trained model to the real data.

The synthetic data consist of three components: stochastic noise with a pinkish-red spectrum, linear drift with random amplitude, and artificial SSE ramps with random duration and amplitude (He et al., 2020) (Fig. S6). This study is improved by including both up-ramp and down-ramp synthetic SSE signals, representing the subsidence and uplift in the pressure. A shallow SSE can cause both surface uplift and subsidence on the seafloor (Fredrickson et al., 2019). The total number of synthetic training data is 0.56 million. We trained the machine learning model on synthetic data with a 3-5 dB signal-to-noise ratio. This means that if the standard deviation of background pressure noise is 1 hPa (1 cm), the target amplitude of the SSE is 2.5-4.3 cm. In this study, the standard deviation of each piece of data ranges from ~1-4 hPa so that the target amplitude ranges between 2.5 and 17.2 cm. Other parameter settings are the same as in our previous study (He et al., 2020).

The deep learning model includes convolutional and recurrent neural networks, which can extract and study the long and short-term patterns in time series data (Fig. S7). The input is a piece of 60-days normalized pressure difference data from one station. The final layer of the network outputs a vector of probabilities of uplift, subsidence, and no SSE (Fig. S7). The trained model accuracy reaches 80% on synthetic data (Fig. S8).

2.3. Earthquake detection

In order to better observe the relationship between SSEs and seismicity, we built a more detailed earthquake catalog for the entire study region. In addition to the AACSE OBS data, we also used seismic data from nearby on land seismic stations. To build the seismicity catalog, a recursive short-time-average/long-timeaverage (STA/LTA) algorithm (Withers et al., 1998) was used to detect possible earthquakes on individual seismometer channels, after filtering the data between 2 and 10 Hz. We used the Southern Alaska 1D velocity model, also called as the SCAK model (Table S1 & S2), for the earthquake localization. An example of an earthquake in the SSE region detected by our method but not in the USGS catalog is shown in Fig. S9. This event has one of the smallest recording station numbers, comparing with other events in the same region. After the earthquakes were located, we launched a re-association process for the events to better constrain their locations (X. Wei et al., 2022). More details of the earthquake detection method can be found in the supplementary materials (Text S1).

3. Results

3.1. SSE detection

We applied our machine learning detector trained by synthetic data to the processed AACSE pressure data. The pressure time series is split into 60-day sliding windows with 1-day sliding increments and each piece of 60-day data is normalized by its standard deviation. The machine learning detector can calculate the probability of subsidence or uplift in the middle part of the data. A probability of one indicates the highest probability that the 60-day segment contains an SSE. To distinguish the uplift and subsidence detection results, we used minus one to represent the highest probability of subsidence of the seafloor. According to the machine learning threshold test (Fig. S8 c & d), we chose 0.6 as the decision threshold. The detector defines an event when the absolute value of the probability is over 0.6. All the predicted probabilities are organized into the time series shown in Fig. 2B. An animation shows the spatial distribution of the detected results can be found in the supplementary materials (Movie S1). Three screenshots from the movie are shown in Fig. 3.

The detection results show two types of spatial patterns. The first is where most stations show the same trend over a short time range. An example of this pattern is evident around June and July 2018, when over half of the stations show an apparent subsidence signal (Fig. 3A & 3B). This pattern of spatially coherent signals has an along-strike distance of several hundred kilometers. Because of its large-scale spatial coherence, it is likely caused by large-scale ocean circulation patterns that have not been fully eliminated by our data processing. The second pattern evident in our data occurs around Oct. 28, 2018, and shows subsidence at stations LT09, LT10, LT12, and LT19 and uplift at stations LA25, LA26, LA28, and LA30 (Fig. 2C,D & Fig. 3C). This spatial pattern looks more like an SSE than oceanographic waves. Although station LA39 located several hundred kilometers to the east also shows uplift during this period, the two near-trench stations between LA39 and the uplift stations, LA22 and LA23, do not show uplift. The uplift of LA39 is likely a coincidence.

To better understand the proposed SSE displacement pattern, we calculated the expected seafloor deformation from an SSE using Pylith, an open-source finite-element code (Aagaard et al., 2013) (Text S2). A model centered at 55.07N, 156.82W (depth range of 8-20 km) with a slip direction of 20 degrees from north (counterclockwise) can reproduce the observed spatial pattern (Fig. 1 & Fig. 3C,D & Fig. S10) with the uplift (3-4 cm) close to the trench and the subsidence (1-2 cm) further away from the trench. The

slip direction is very close to the subduction direction. The amplitude of the subsidence at stations LT09 and LT14 in the simulated model is smaller than evident in the data. This may be due to the simple assumption of the shape of the SSE. A finite fault inversion could help to better constrain the SSE area, but is beyond the scope of this study. Our simple model predicts very small deformation (<1 mm) that are not observable at the inland GNSS stations, which is consistent with GNSS data (Fig. S11). Our model predicts a maximum slip of 15 cm, equivalent to 2.5 years of accumulated strain

3.2. Seismicity pattern

SSEs can trigger small earthquakes in nearby regions (Nishikawa and Ide, 2018; Vallée et al., 2013; Yarce et al., 2019). Between June 10th and June 24th of 2019, many airgun shots occurred in our SSE region (Barcheck et al., 2020). Thus, we masked this period in Fig. 4A to avoid possible false earthquake detections. We also show the USGS catalog as a comparison. When there are AACSE and other sources of earthquakes in the USGS catalog, we chose the AACSE as the first choice for the earthquake locations and origin times. The total number of detected earthquakes in our catalog is about three times of that in the USGS catalog.

Daily seismicity rates show an increase of seismicity in this area right after the SSE (Fig. 4A). We counted the number of earth-quakes within a 120-km radius circle centered at 55°N, 157°W. The daily seismicity rate increases by a factor of three in the ten days right after the SSE compared to during the SSE in both the USGS catalog and our study. The elevated seismicity occurred on the up-dip, down-dip ends, and to the west of the inferred SSE area (Fig. 4B), likely triggered by the SSE. Additionally, the seismicity rate drops about 25 percent from the previous rate in the ten months after Nov.20, 2018 (Fig. 4A). There are two rate peaks before the SSE. The increased seismicity near July 24th, 2018, is due to a Mw 4.5 main shock and its aftershocks. There is no main shock for the peak on August 13th, 2018. The magnitude of seismicity is smaller than 3 and earthquakes are sparsely distributed.

Earthquake swarms associated with shallow SSEs have been observed in New Zealand, Japan, and Ecuador (Bartlow et al., 2014; Montgomery-Brown and Syracuse, 2015; Nishikawa and Ide, 2018; Reverso et al., 2016; Vallée et al., 2013). In these studies, some swarms occurred before the SSE as foreshocks, and others occurred during or after the SSE. In our case, the earthquake swarms followed the SSE and are located updip and downdip of the SSE (Fig. 4B). We further calculate the Coulomb stress change caused by the SSE using the previously mentioned numerical simulation model. The elevated seismicity is in positive Coulomb stress change regions, consistent with triggering by the SSE (Fig. 4B). We also observed that the epicenters of the 2020 Simeonof earthquake and 2021 Chignik earthquake were in the positive Coulomb stress change regions. The SSE increased the Coulomb stress for the 2021 earthquake by about 0.2 bar and the 2020 earthquake by less than 0.05 bar. The SSE might have advanced the 2021 Chignik earthquake.

3.3. Tremor detection

Often enhanced nonvolcanic tremor activity accompanies SSEs near their source area (Beroza and Ide, 2011; Rousset et al., 2019). In this study, we attempted to detect tremors using land and offshore seismic stations during the AACSE time (see Text S3 for details). Around 20 isolated short-duration (\sim 90 seconds long) tremors were detected near the SSE at stations LA23, LA25 and LD36 (Fig. S1); however, only 3 occurred close in time to the SSE on Oct.7 (Fig. S13).

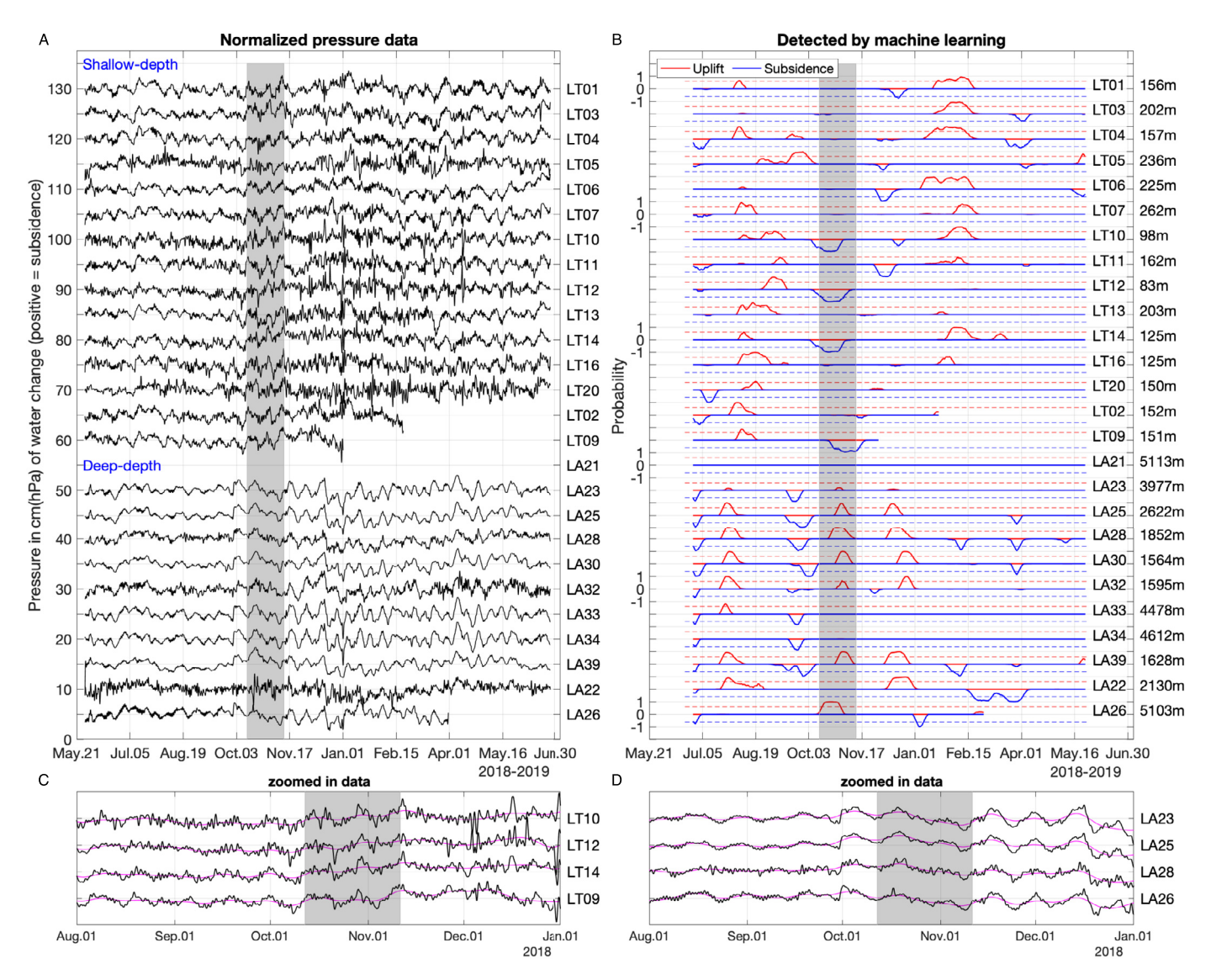


Fig. 2. Normalized pressure data and machine learning detection results. (A). Shallow-water and deep-water normalized pressure data. (B). Detected probabilities from each station. All the detected probabilities (red and blue) vary within $0 \sim \pm 1$. Red and blue dashed lines represent the detection thresholds of ± 0.6 , respectively. Only the probabilities over the thresholds are considered as an uplift or subsidence signal. (C)(D). The zoom-in panels of pressure data in Fig. 3C. The gray shaded region highlights the SSE time from Oct. 13 to Nov. 11, 2018. The magenta lines are the trace of 15-day low-pass filtered data to show the long-wavelength nature of the SSE.

The lack of enhanced tremor activity can be due to the sparse station distribution, noisy OBS data, small amplitude tremors, and fewer tremors in this area (Montgomery-Brown and Syracuse, 2015). The station spacing in AACSE is 20-40 km, and we require at least three stations to detect a tremor. It is possible that only one or two stations captured some tremors, and we could not identify them. Additionally, noise is much higher (between 1 and 8 Hz) in the OBS data compared to the land stations (Barcheck et al., 2020). It is hard to detect small tremors from OBS data (Wech et al., 2013). Lastly, it is possible that tremors are just not abundant in this SSE area. This has been observed elsewhere; no tremor was detected during the 2013 Boso Peninsula SSE, although the region was densely instrumented at this time (Montgomery-Brown and Syracuse, 2015).

4. Discussion

4.1. The relation between the SSE and earthquakes

Our detected SSE occurred between Oct. 12 and Nov. 11 of 2018 with 5 – 10 days of uncertainty. The machine learning detector

cannot estimate the amplitude of vertical deformation. According to our simple SSE forward model, the maximum slip during the SSE is 15 cm and the moment magnitude is 6.9. Assuming a subduction rate of 60 cm/year and full release of stress by the SSEs at this location, it would take another 2-3 years for the next SSE to occur at this location in the Semidi segment. The two earthquake swarms after the SSE might be triggered by the SSE but also could be unrelated (Fig. 4A). We are unable to detect smaller earthquakes (Mw<2) because of the low signal to noise ratio of the OBS.

On July 22, 2020, the Mw 7.8 Simeonof earthquake occurred on the Shumagin segment, located about 150 km southwest of the SSE area (Fig. 1). The Mw 8.1 2021 Chignik main shock occurred on the Semidi segment in July. This event had a hypocentral depth of 32.2 km and fault slip models all indicate that the earthquake did not rupture the shallow portion of the plate interface; most of the slip occurred at depths of 20-40 km (Liu et al., 2022; Ye et al., 2022). In contrast, the 1938 Mw 8.3 earthquake occurred just east of the 2021 Chignik earthquake but ruptured to a much shallower depth and generated an intermediate sized tsunami (Freymueller et al., 2021). The lack of shallow slip during the 2021 earthquake is consistent with the occurrence of an SSEs in this area that pre-

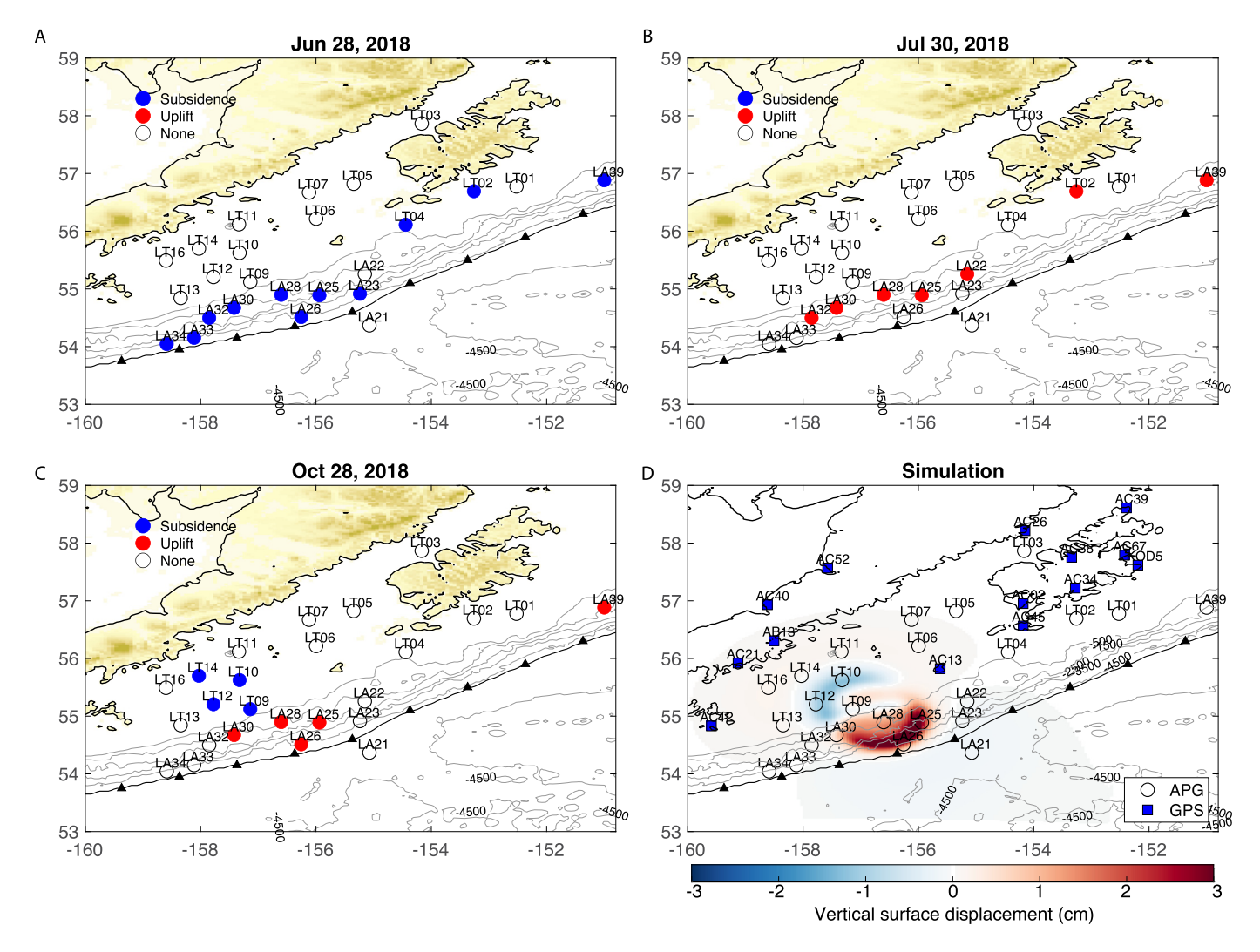


Fig. 3. Detection snapshots and simulation. (A, B, C) The detection of apparent vertical deformation at three dates. More detected results are shown in the Movie S1. (D) Simulated surface displacement of an SSE on the thrust interface. Red and blue represent uplift and subsidence, respectively.

released the stress accumulation in the shallow Semidi subduction zone. In addition, the epicenter of both the 2020 Simeonof and the 2021 Chignik events locate in positive Coulomb stress change regions following the 2018 SSE.

A 10-year analysis of the b-value in this area shows that the SSE occurred in a region with a low b-value (Liu et al., 2020). Variations of the b-value can be interpreted as the presence of asperities and variable frictional properties (Schorlemmer and Wiemer, 2005). A decrease in b-value also indicates the high-stress accumulation and potential large earthquake location (Nanjo et al., 2012; Schorlemmer et al., 2005). In the west Semidi segment, Liu et al. (2020) found the b-value gradually decreased from 0.95 to below 0.8 since 2011, which can be related to the nucleation of the 2021 Chignik earthquake. They also observed that the b-value rebounded from 0.7 to 0.75 at the end of 2018. The rebound might have been caused by the stress released by the 2018 SSE.

4.2. The uncertainties of detected SSE

In order to assure that our detected SSE is not due to oceanographic sources we ran the machine learning algorithm on data generated using the oceanic circulation model HYCOM for this region from 2010-2019. We calculated the seafloor pressure by subtracting the integral of the upper water column's density from the sea surface height. To resemble the real data processing steps, we subtracted different global means from the shallow-water (0-500 m) and (500–4500 m) deep-water stations, and then put the pressure residuals at each station into the machine learning algorithm. The detector indeed finds some periods of subsidence and uplift (Movie. S2). For example, stations closely located show identical signals because common wave signals are left in the pressure residuals. Also, one or two stations may show paired uplift and subsidence due to noise or small eddies. However, we did not find a single case with multiple stations showing a pattern similar to our detected SSE. Therefore, our SSE pattern does not likely result from an oceanographic process.

4.3. Geological and physical conditions for SSE in this region

The occurrence of shallow SSEs has been attributed to several factors: (1) abundant fluids; (2) high fault roughness and heterogeneous fault structure; (3) being near the transition zone in frictional properties; and (4) modestly unstable fault patches smaller than the critical dimension needed for earthquake nucleation (Bürgmann, 2018; Saffer and Wallace, 2015). In the Semidi segment, trace element analysis in nearby volcanoes shows that there is less fluid in the Semidi segment compared to the Shumagin segment in the deep subduction zone (>100 km) (S. S. Wei et al., 2021). However, the fluid status is unclear in the shallow Semidi segment. There are several bending faults visible on a seis-

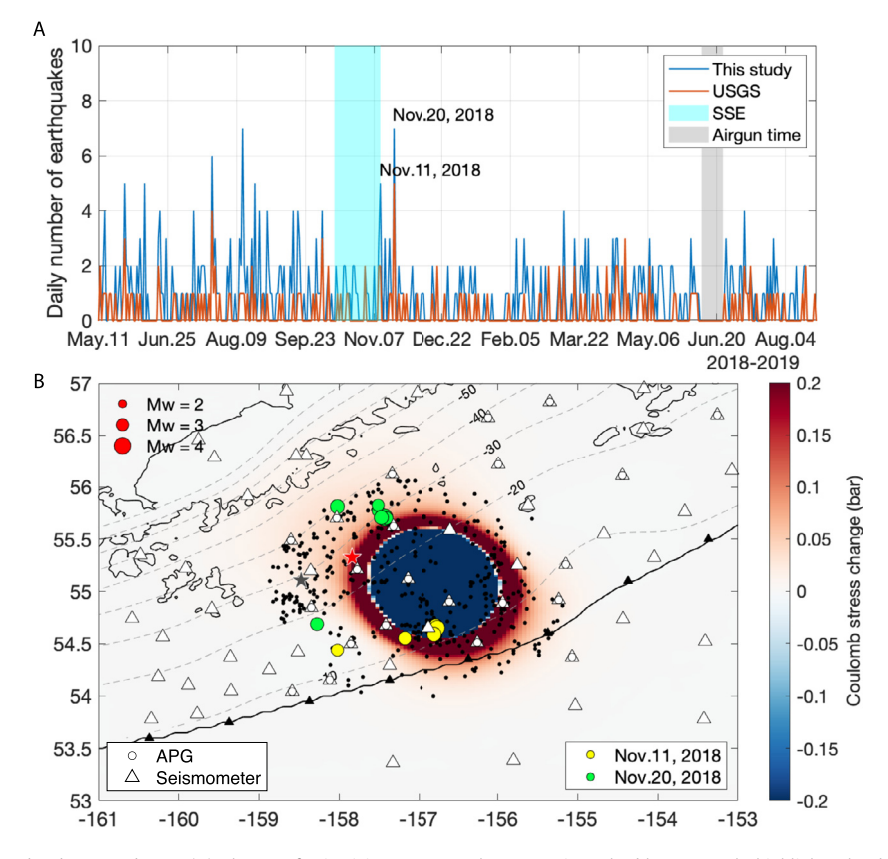


Fig. 4. Daily earthquakes and coulomb stress change (A) Change of seismicity rate near the SSE region. The blue rectangle highlights the duration of the SSE. The gray bar masks the airgun shot time. (B) Coulomb stress change of the SSE. The yellow and green dots show the earthquake swarm after the SSE. The background black dots are the seismicity after the SSE time (Nov. 10, 2018-Aug. 24, 2019). Figure S12 shows the background seismicity with a scale of the Moment magnitude and two earthquake swarms before SSE. The gray and red stars label the epicenters of the 2020 Simeonof earthquake and 2021 Chignik earthquake, respectively.

Thick Zodiac Fan sediments (~800-m) and other pelagic sediments subduct along the Semidi segment (Stevenson et al., 1983). However, such thick sediment cannot bury the subducting Patton-Murray ridge, whose height is over 1 km. In the west of the Semidi segment, a buried extension of the subducting Patton-Murray Ridge was recognized. It created a ridge or escarpment terminating the continental shelf and an embayment in the accretionary front (Fig. 1) (von Huene et al., 2016). These geological features are unique to the Semidi segment and thought to be favorable for tsunami hosting earthquakes (von Huene et al., 2016). The physical conditions for tsunami hosting earthquakes and shallow SSEs are similar (Saffer and Wallace, 2015), so the Semidi segment may also favor shallow SSEs. The buried extension of the subducting Patton-Murray Ridge decreases effective normal stress, elevates pore fluid pressure, and may facilitate slow slip in the fault zone.

There are many seismic reflection studies between Kodiak and the Shumagin Islands. Detailed fault structure they reveal can help delineate different portions of the seismogenic zone. In the west Semidi segment, a thin sharp reflection with a single low-velocity zone is observed at a depth of 13 to 20 km, it has been interpreted as the frictionally unstable region (J. Li et al., 2015). In our SSE simulation result, significant slip is also found in this depth range, so our proposed SSE may represent failure of a velocity-strengthening (stable) to weakening (unstable) fault patch. The fault patch may be over-pressured and slip as SSEs due to a combination of trapping fluids and disequilibrium compaction.

5. Conclusion

We applied a newly developed machine learning method to detect SSEs in seafloor pressure data between the summers of 2018 and 2019 offshore southern Alaska. The method detected one event between Oct. 13 and Nov. 11, 2018 with 5 to 10 days of uncertainty. The spatial pattern of the deformation is unlikely oceanographic in origin, based on analysis of 10-years of model output from the global numerical circulation model HYCOM. The pattern is consistent with simulated ground deformation resulting from slow slip on an oval-shaped patch on the subduction interface. Our detected SSE is located 150-km northeast of the 2020 Mw 7.8 Alaska earthquake and updip of the 2021 Mw 8.2 Chignik earthquake. Neither earthquake ruptured to shallow depth, or generated a significant tsunami, consistent with our observation of a shallow SSEs in this region that released tectonic stresses accumulated on the shallow plate interface. Our method has the potential to transform the way SSE are identified in seafloor pressure data allowing SSE far from the shoreline to be detected.

CRediT authorship contribution statement

Bing He: Conceptualization, SSE detection, Tremor detection, Machine learning model design, Visualization Writing – original draft, Writing – review & editing.

XiaoZhuo Wei: Earthquake detection, Visualization, Writing – review & editing.

Meng (Matt) Wei: Conceptualization, SSE detection, Tremor detection, Visualization, Writing – review & editing.

Yang Shen: Earthquake detection, Writing – review & editing.

Marco Alvarez: Machine learning model design, Writing – review & editing.

Susan Y. Schwartz: Tremor detection, Writing – review & editing.

Declaration of competing interest

The authors declare that they have no known competing financial interests or personal relationships that could have appeared to influence the work reported in this paper.

Data and materials availability

AACSE seismic and pressure data can be downloaded from ISRS. The earthquake catalog is from USGS website. The HYCOM data are from HYCOM website (https://www.hycom.org/dataserver/gofs-3pt1/reanalysis). The ECCO4 data are from NASA ECCO website (https://podaac.jpl.nasa.gov/ECCO?tab=mission-objectives§ions=about%2Bdata). High-resolution bathymetry data are from GMRT website (https://www.gmrt.org/GMRTMapTool/). Most of the data processing, calculations, and figures are carried out using MATLAB and PYTHON. The machine learning code was written with Python packages Keras (https://keras.io/) and Scikit-learn (https://sci-kit-learn.org/stable/). The machine learning model can be found in github (https://github.com/bing-he/SSE_detection_using_machine_learning).

Acknowledgements

We sincerely thank Randolph Watts and Karen Tracey for the guidance on analyzing seafloor pressure data, Natalia Ruppert for providing velocity models of Alaskan-Aleutian subduction zone, Jiuxun Yin and Noel Bartlow for their constructive and productive discussion, and Sandra Slead for proof reading. We are grateful to the PIs and staffs of the AACSE for providing the Alaska ocean bottom pressure and seismic data. This project is supported by the National Science Foundation of United States (Award #2025563 and #1949620).

Appendix A. Supplementary material

Supplementary material related to this article can be found online at https://doi.org/10.1016/j.epsl.2023.118154.

References

- Aagaard, B.T., Knepley, M.G., Williams, C.A., 2013. A domain decomposition approach to implementing fault slip in finite-element models of quasi-static and dynamic crustal deformation. J. Geophys. Res., Solid Earth 118 (6), 3059–3079. https://doi.org/10.1002/jgrb.50217.
- Araki, E., Saffer, D.M., Kopf, A.J., Wallace, L.M., Kimura, T., Machida, Y., et al., 2017. Recurring and triggered slow-slip events near the trench at the Nankai Trough subduction megathrust. Science 356 (6343), 1157–1160. https://doi.org/10.1126/science.aan3120.
- Barcheck, G., Abers, G.A., Adams, A.N., Bécel, A., Collins, J., Gaherty, J.B., et al., 2020. The Alaska amphibious community seismic experiment. Seismol. Res. Lett. 91 (6), 3054–3063. https://doi.org/10.1785/0220200189.

- Bartlow, N.M., Wallace, L.M., Beavan, R.J., Bannister, S., Segall, P., 2014. Time-dependent modeling of slow slip events and associated seismicity and tremor at the Hikurangi subduction zone, New Zealand. J. Geophys. Res., Solid Earth 119 (1), 734–753. https://doi.org/10.1002/2013JB010609.
- Beroza, G.C., Ide, S., 2011. Slow earthquakes and nonvolcanic tremor. Annu. Rev. Earth Planet. Sci. 39 (1), 271–296. https://doi.org/10.1146/annurev-earth-040809-152531.
- Bürgmann, R., 2018. The geophysics, geology and mechanics of slow fault slip. Earth Planet. Sci. Lett. 495, 112–134. https://doi.org/10.1016/j.epsl.2018.04.062.
- Crowell, B.W., Melgar, D., 2020. Slipping the Shumagin Gap: a kinematic coseismic and early afterslip model of the Mw 7.8 Simeonof Island, Alaska, earth-quake. Geophys. Res. Lett. 47 (19), e2020GL090308. https://doi.org/10.1029/2020GL090308
- Davies, J., Sykes, L., House, L., Jacob, K., 1981. Shumagin Seismic Gap, Alaska Peninsula: history of great earthquakes, tectonic setting, and evidence for high seismic potential. J. Geophys. Res., Solid Earth 86 (B5), 3821–3855. https:// doi.org/10.1029/JB086iB05p03821.
- Davis, E.E., Villinger, H., Sun, T., 2015. Slow and delayed deformation and uplift of the outermost subduction prism following ETS and seismogenic slip events beneath Nicoya Peninsula, Costa Rica. Earth Planet. Sci. Lett. 410, 117–127. https:// doi.org/10.1016/j.epsl.2014.11.015.
- Dixon, T.H., Jiang, Y., Malservisi, R., McCaffrey, R., Voss, N., Protti, M., Gonzalez, V., 2014. Earthquake and tsunami forecasts: relation of slow slip events to subsequent earthquake rupture. Proc. Natl. Acad. Sci. 111 (48), 17039–17044.
- Fredrickson, E.K., Wilcock, W.S.D., Schmidt, D.A., MacCready, P., Roland, E., Kurapov, A.L., et al., 2019. Optimizing sensor configurations for the detection of slow-slip earthquakes in seafloor pressure records, using the Cascadia Subduction Zone as a case study. J. Geophys. Res., Solid Earth 124 (12), 13504–13531. https://doi.org/10.1029/2019JB018053.
- Freymueller, J.T., Suleimani, E.N., Nicolsky, D.J., 2021. Constraints on the slip distribution of the 1938 MW 8.3 Alaska Peninsula earthquake from tsunami modeling. Geophys. Res. Lett. 48 (9), e2021GL092812. https://doi.org/10.1029/2021GL092812.
- Gomberg, J., Hautala, S., Johnson, P., Chiswell, S., 2019. Separating sea and slow slip signals on the seafloor. J. Geophys. Res., Solid Earth 124 (12), 13486–13503. https://doi.org/10.1029/2019/B018285.
- Hayes, G.P., Moore, G.L., Portner, D.E., Hearne, M., Flamme, H., Furtney, M., Smoczyk, G.M., 2018. Slab2, a comprehensive subduction zone geometry model. Science 362 (6410), 58–61.
- He, B., Wei, M., Watts, D.R., Shen, Y., 2020. Detecting slow slip events from seafloor pressure data using machine learning. Geophys. Res. Lett. 47 (11), e2020GL087579. https://doi.org/10.1029/2020GL087579.
- Hino, R., Inazu, D., Ohta, Y., Ito, Y., Suzuki, S., Iinuma, T., et al., 2014. Was the 2011 Tohoku-Oki earthquake preceded by aseismic preslip? Examination of seafloor vertical deformation data near the epicenter. Mar. Geophys. Res. 35 (3), 181–190. https://doi.org/10.1007/s11001-013-9208-2.
- von Huene, R., Miller, J.J., Dartnell, P., 2016. A possible transoceanic tsunami directed toward the U.S. west coast from the Semidi segment, Alaska convergent margin. Geochem. Geophys. Geosyst. 17 (3), 645–659. https://doi.org/10.1002/2015GC006147.
- Inazu, D., Hino, R., Fujimoto, H., 2012. A global barotropic ocean model driven by synoptic atmospheric disturbances for detecting seafloor vertical displacements from in situ ocean bottom pressure measurements. Mar. Geophys. Res. 33 (2), 127–148. https://doi.org/10.1007/s11001-012-9151-7.
- Ito, Y., Hino, R., Kido, M., Fujimoto, H., Osada, Y., Inazu, D., et al., 2013. Episodic slow slip events in the Japan subduction zone before the 2011 Tohoku-Oki earthquake. Tectonophysics 600, 14–26. https://doi.org/10.1016/j.tecto.2012.08.022.
- Li, J., Shillington, D.J., Bécel, A., Nedimović, M.R., Webb, S.C., Saffer, D.M., et al., 2015. Downdip variations in seismic reflection character: implications for fault structure and seismogenic behavior in the Alaska subduction zone. J. Geophys. Res., Solid Earth 120 (11), 7883–7904. https://doi.org/10.1002/2015JB012338.
- Li, J., Shillington, D.J., Saffer, D.M., Bécel, A., Nedimović, M.R., Kuehn, H., et al., 2018. Connections between subducted sediment, pore-fluid pressure, and earthquake behavior along the Alaska megathrust. Geology 46 (4), 299–302. https://doi.org/ 10.1130/G39557.1.
- Li, S., Freymueller, J.T., 2018. Spatial variation of slip behavior beneath the Alaska Peninsula along Alaska-Aleutian subduction zone. Geophys. Res. Lett. 45 (8), 3453–3460. https://doi.org/10.1002/2017GL076761.
- Li, S., Freymueller, J., McCaffrey, R., 2016. Slow slip events and time-dependent variations in locking beneath Lower Cook Inlet of the Alaska-Aleutian subduction zone. J. Geophys. Res., Solid Earth 121 (2), 1060–1079. https://doi.org/10.1002/2015JB012491.
- Lindsey, E.O., Mallick, R., Hubbard, J.A., Bradley, K.E., Almeida, R.V., Moore, J.D.P., et al., 2021. Slip rate deficit and earthquake potential on shallow megathrusts. Nat. Geosci. 14 (5), 321–326. https://doi.org/10.1038/s41561-021-00736-x.
- Liu, C., Lay, T., Xiong, X., Wen, Y., 2020. Rupture of the 2020 MW 7.8 earthquake in the Shumagin Gap inferred from seismic and geodetic observations. Geophys. Res. Lett. 47 (22), e2020GL090806. https://doi.org/10.1029/2020GL090806.
- Liu, C., Lay, T., Xiong, X., 2022. The 29 July 2021 MW 8.2 Chignik, Alaska Peninsula earthquake rupture inferred from seismic and geodetic observations: re-

- rupture of the western 2/3 of the 1938 rupture zone. Geophys. Res. Lett. 49 (4), e2021GL096004. https://doi.org/10.1029/2021GL096004.
- Montgomery-Brown, E.K., Syracuse, E.M., 2015. Tremor-genic slow slip regions may be deeper and warmer and may slip slower than non-tremor-genic regions. Geochem. Geophys. Geosyst. 16 (10), 3593–3606. https://doi.org/10.1002/ 2015GC005895
- Munk, W.H., Cartwright, D.D., Bullard, E.C., 1966. Tidal spectroscopy and prediction. Philos. Trans. R. Soc. Lond. Ser. A, Math. Phys. Sci. 259 (1105), 533–581. https://doi.org/10.1098/rsta.1966.0024.
- Muramoto, T., Ito, Y., Inazu, D., Wallace, L.M., Hino, R., Suzuki, S., et al., 2019. Seafloor crustal deformation on ocean bottom pressure records with nontidal variability corrections: application to Hikurangi margin, New Zealand. Geophys. Res. Lett. 46 (1), 303–310. https://doi.org/10.1029/2018GL080830.
- Nanjo, K.Z., Hirata, N., Obara, K., Kasahara, K., 2012. Decade-scale decrease inb value prior to the M9-class 2011 Tohoku and 2004 Sumatra quakes. Geophys. Res. Lett. 39 (20). https://doi.org/10.1029/2012GL052997.
- Nishikawa, T., Ide, S., 2018. Recurring slow slip events and earthquake nucleation in the source region of the M 7 Ibaraki-Oki earthquakes revealed by earthquake swarm and foreshock activity. J. Geophys. Res., Solid Earth 123 (9), 7950–7968. https://doi.org/10.1029/2018/B015642.
- Reverso, T., Marsan, D., Helmstetter, A., Enescu, B., 2016. Background seismicity in Boso Peninsula, Japan: long-term acceleration, and relationship with slow slip events. Geophys. Res. Lett. 43 (11), 5671–5679. https://doi.org/10.1002/2016GL068524.
- Rousset, B., Fu, Y., Bartlow, N., Bürgmann, R., 2019. Weeks-long and years-long slow slip and tectonic tremor episodes on the south central Alaska megathrust. J. Geophys. Res., Solid Earth 124 (12), 13392–13403. https://doi.org/10. 1029/2019/B018724.
- Ruiz, S., Metois, M., Fuenzalida, A., Ruiz, J., Leyton, F., Grandin, R., et al., 2014. Intense foreshocks and a slow slip event preceded the 2014 Iquique Mw 8.1 earthquake. Science 345 (6201), 1165–1169. https://doi.org/10.1126/science.1256074.
- Saffer, D.M., Wallace, L.M., 2015. The frictional, hydrologic, metamorphic and thermal habitat of shallow slow earthquakes. Nat. Geosci. 8 (8), 594–600. https://doi.org/10.1038/ngeo2490.
- Schorlemmer, D., Wiemer, S., 2005. Microseismicity data forecast rupture area. Nature 434 (7037), 1086. https://doi.org/10.1038/4341086a.
- Schorlemmer, D., Wiemer, S., Wyss, M., 2005. Variations in earthquake-size distribution across different stress regimes. Nature 437 (7058), 539–542. https://doi.org/10.1038/nature04094.
- Shillington, D.J., Bécel, A., Nedimović, M.R., Kuehn, H., Webb, S.C., Abers, G.A., et al., 2015. Link between plate fabric, hydration and subduction zone seismicity in Alaska. Nat. Geosci. 8 (12), 961–964. https://doi.org/10.1038/ngeo2586.
- Stevenson, A.J., Scholl, D.W., Vallier, T.L., 1983. Tectonic and geologic implications of the Zodiac fan, Aleutian Abyssal Plain, northeast Pacific. Geol. Soc. Am. Bull. 94 (2), 259–273. https://doi.org/10.1130/0016-7606(1983)94<259:TAGIOT>2.0.CO;2.

- Vallée, M., Nocquet, J.-M., Battaglia, J., Font, Y., Segovia, M., Régnier, M., et al., 2013. Intense interface seismicity triggered by a shallow slow slip event in the Central Ecuador subduction zone. J. Geophys. Res., Solid Earth 118 (6), 2965–2981. https://doi.org/10.1002/jgrb.50216.
- Wallace, L.M., Webb, S.C., Ito, Y., Mochizuki, K., Hino, R., Henrys, S., et al., 2016. Slow slip near the trench at the Hikurangi subduction zone, New Zealand. Science 352 (6286), 701–704.
- Watts, D.R., Kontoyiannis, H., 1990. Deep-ocean bottom pressure measurement: drift removal and performance. J. Atmos. Ocean. Technol. 7 (2), 296–306. https://doi.org/10.1175/1520-0426(1990)007<0296:DOBPMD>2.0.CO;2.
- Wech, A.G., Sheehan, A.F., Boese, C.M., Townend, J., Stern, T.A., Collins, J.A., 2013. Tectonic tremor recorded by ocean bottom seismometers. Seismol. Res. Lett. 84 (5), 752–758. https://doi.org/10.1785/0220120184.
- Wei, M., McGuire, J.J., Richardson, E., 2012. A slow slip event in the south central Alaska Subduction Zone and related seismicity anomaly. Geophys. Res. Lett. 39 (15). https://doi.org/10.1029/2012GL052351.
- Wei, S.S., Ruprecht, P., Gable, S.L., Huggins, E.G., Ruppert, N., Gao, L., Zhang, H., 2021. Along-strike variations in intermediate-depth seismicity and arc magmatism along the Alaska Peninsula. Earth Planet. Sci. Lett. 563, 116878. https:// doi.org/10.1016/j.epsl.2021.116878.
- Wei, X., Shen, Y., Caplan-Auerbach, J., Morgan, J.K., 2022. An improved earthquake catalog during the 2018 Kīlauea eruption from combined onshore and offshore seismic arrays. Earth Space Sci. 9 (6), https://doi.org/10.1029/2021EA001979.
- Withers, M., Aster, R., Young, C., Beiriger, J., Harris, M., Moore, S., Trujillo, J., 1998. A comparison of select trigger algorithms for automated global seismic phase and event detection. Bull. Seismol. Soc. Am. 88 (1), 95–106. https://doi.org/10.1785/BSSA0880010095.
- Xiao, Z., Freymueller, J.T., Grapenthin, R., Elliott, J.L., Drooff, C., Fusso, L., 2021. The deep Shumagin gap filled: kinematic rupture model and slip budget analysis of the 2020 Mw 7.8 Simeonof earthquake constrained by GNSS, global seismic waveforms, and floating InSAR. Earth Planet. Sci. Lett. 576, 117241. https://doi. org/10.1016/j.epsl.2021.117241.
- Yarce, J., Sheehan, A.F., Nakai, J.S., Schwartz, S.Y., Mochizuki, K., Savage, M.K., et al., 2019. Seismicity at the northern Hikurangi margin, New Zealand, and investigation of the potential spatial and temporal relationships with a shallow slow slip event. J. Geophys. Res., Solid Earth 124 (5), 4751–4766. https://doi.org/10.1029/2018JB017211.
- Ye, L., Lay, T., Kanamori, H., Yamazaki, Y., Cheung, K.F., 2021. The 22 July 2020 MW 7.8 Shumagin seismic gap earthquake: partial rupture of a weakly coupled megathrust. Earth Planet. Sci. Lett. 562, 116879. https://doi.org/10.1016/j. epsl.2021.116879.
- Ye, L., Bai, Y., Si, D., Lay, T., Cheung, K.F., Kanamori, H., 2022. Rupture model for the 29 July 2021 MW 8.2 Chignik, Alaska earthquake constrained by seismic, geodetic, and tsunami observations. J. Geophys. Res., Solid Earth 127 (7), e2021|B023676. https://doi.org/10.1029/2021|B023676.